Letter

Real-space detection and manipulation of two-dimensional quantum well states in few-layer MoS_2

Yu Wang,[1,3,*] Linlu Wu,[2,*] Zheng Wei,[1,3] Zijia Liu,[1,3] Peng Cheng,[1,3] Yiqi Zhang,[1,3] Baojie Feng,[1,3] Guangyu Zhang,[1,3,4] Wei Ji,[2,†] Kehui Wu,[1,3,4,‡] and Lan Chen[1,3,4,§]

[1]*Institute of Physics, Chinese Academy of Sciences, Beijing 100190, China*
[2]*Department of Physics, Renmin University of China, Beijing 100872, China*
[3]*School of Physical Sciences, University of Chinese Academy of Sciences, Beijing 100190, China*
[4]*Songshan Lake Materials Laboratory, Dongguan, Guangdong 523808, China*

(Received 13 December 2020; revised 24 January 2022; accepted 26 January 2022; published 8 February 2022)

Quantum confinement has remarkable effects on the band structures and optoelectronic performance of semiconducting materials. The confinement of electronic states developed along van der Waals (vdW) gaps in transition metal dichalcogenides (TMDs) has unique advantages compared with those of artificial quantum wells. Here, we detected the quantized electronic states of few-layered MoS_2 in real space using scanning tunneling microscope/spectroscopy. Combined with density-functional theory calculations, the quantized states were attributed to quantum-well states (QWSs), and the number of the states was strictly determined by the MoS_2 layer thickness. We further regulated the QWSs of few-layered MoS_2 by tuning the strength of interlayer hybridization through directly adjusting the interlayer distance. More importantly, substitutional defects in few-layered MoS_2 were introduced to control the energy eigenvalues of the QWSs. Our work proves the existence of the interlayer electronic hybridization in conventional weakly coupled vdW interfaces, and provides a way to manipulate the electronic states of few-layered TMD through controlling interlayer hybridization. It also suggests potential applications of quantum-well materials in subband transitions, spin splitting, photoexcitation, and electronic devices.

DOI: 10.1103/PhysRevB.105.L081404

The quantum confinement of charge carriers gives rise to a variety of exotic physical phenomena and plays an important role in many applications. For example, quantum confinement can modulate thin-film growth [1–3] and induce phenomena such as the semiconductor-metal transition [4], tunable superconductivity [5,6], and surface reactivity [7]. In conventional metal thin films, the quantum confinement of free electrons between the top and bottom surfaces gives rise to vertical quantum-well states (QWSs). These are well understood and have been directly probed by surface-sensitive tools such as angle-resolved photoelectron emission spectroscopy and scanning tunneling spectroscopy (STS) [8,9].

However, in recently discovered two-dimensional (2D) layered materials such as transition-metal dichalcogenides (TMDs) [10] and their heterojunctions [Fig. 1(a)], this picture becomes less straightforward. Since these materials are usually semiconductors, and different layers are only weakly coupled by van der Waals (vdW) interactions, carriers in layered TMDs are mostly confined within individual layers. In this case, the formation of 2D QWSs perpendicular to the surface is better described by the hybridization and redistribution of degenerate electron states in different layers through strong interlayer hybridization [Fig. 1(b)]. This picture has been theoretically discussed and is believed to be related to various experimental phenomena in TMDs, e.g., valence band splitting [11,12], thickness-dependent band gap [13,14], intersubband excitation and transitions [15], indirect-direct band-gap transitions [16,17], and interlayer hybridization and band offset of 2D vdW heterojunctions [18,19]. Two-dimensional QWSs also strongly influence the electronic and optoelectronic applications of 2D layered materials and their heterostructures [20–22]. For example, the electronic band gaps of black phosphorus [23] and some group-10 TMDs, e.g., PtS_2 [24] and $PtSe_2$ [25], exhibit apparent layer dependence, which may be ascribed to the formation of 2D QWSs. Nevertheless, it is still under debate whether QWSs exist in weakly interlayer-coupled TMDs, e.g., MoS_2 [26–30]; it is thus desirable to directly confirm and manipulate 2D QWSs of MoS_2 in real space.

Here, we report the direct observation of QWSs in few-layered MoS_2 films by probing the local density of states (LDOS) using scanning tunneling microscopy/spectroscopy (STM/STS). The number of LDOS peaks in STS closely corresponds to the number of MoS_2 layers. Density-functional theory (DFT) calculations revealed that these LDOS peaks originated from the 2D QWSs of MoS_2 and reproduced the evolution of 2D QWSs upon increasing the number of layers. Moreover, we adopted two strategies, varying the interlayer distance and inserting oxygen atoms into the sulfur layers, to prove that the behaviors of 2D QWSs (including intensity and energy position) are determined by the interlayer electronic hybridization. Our investigations suggest that the strong

*These authors contributed equally to this work.
†wji@ruc.edu.cn
‡khwu@iphy.ac.cn
§lchen@iphy.ac.cn

 ©2022 American Physical Society

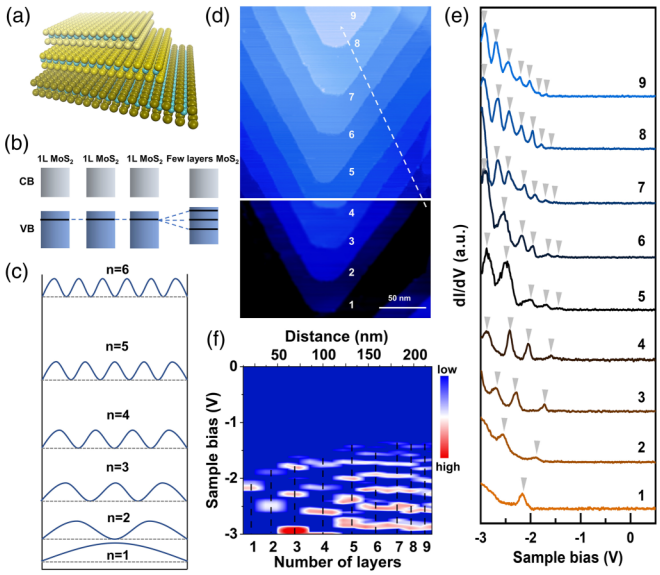

FIG. 1. (a)–(c) Theoretical schematic diagram of 2D vdW quantum-well states. (a) Atomic structure of MoS_2, where the blue balls represent Mo atoms. (b) Diagram of band hybridization. (c) Energy levels and wave functions for a square potential well. Topographic images and scanning tunneling spectra of few-layered MoS_2 for figures (d)–(f). (d) STM image of a MoS_2 island with 9 layers ($200 \times 320\,nm^2$; $V_s = -2.6\,V$, $I_s = 150\,pA$). Due to the scanning process, this image is made up of two images. (e) The dI/dV spectra acquired on each layer MoS_2 surface (1–9 layers), respectively. The gray arrows indicate the position of the corresponding peaks of each layer. (f) The second derivative of the dI/dV color map obtained along the line indicated by the white arrow in (d). A set of black dashed lines marks the peaks corresponding to each layer.

electronic hybridizations can exist in conventional weakly coupled vdW interfaces, leading to the formation of 2D QWSs in few-layered MoS_2. The possibility to manipulate the interface hybridization implies potential applications in semiconductor electronics and optoelectronic devices.

The growth of few-layered MoS_2 films was carried out in a three-temperature zone chemical vapor deposition system. Sulfur powder (Alfa Aesar, 99.5%, 5 g) and MoO_3 powder (Alfa Aesar, 99.9995%, 10 mg) were loaded in two inner quartz tubes in low-temperature zones. Highly oriented pyrolytic graphite (HOPG) was chosen as the substrate and placed in the high-temperature zone. Here, we used Ar and O_2 as the carrier gases. For the inner tube containing S powder, only Ar (200 sccm) was used, while a mixture of Ar (75 sccm) and O_2 (3.5 sccm) was used for the inner tube containing MoO_3 powder. The O atoms substituted for S atoms were derived from O_2. The pressure of the chamber was kept at about 1 Torr. During the growth process, the temperatures were held at 130, 530, and 900 °C for S, MoO_3, and HOPG substrate, and the growth process lasted for ~40 min.

STM and STS data were obtained in a home-built low-temperature molecular-beam epitaxy (MBE)-STM system (base pressure $\sim 10^{-10}$ Torr). Samples were transferred to the MBE chamber through atmosphere. Then, the samples were annealed at approximately 350 K in a vacuum to remove surface-adsorbed impurities. Subsequently, the samples were transmitted directly to the STM chamber without breaking the vacuum. All data were taken at 5 K by a chemically etched tungsten tip, and the bias voltages were defined as the sample bias with respect to the tip. The STM images were processed using free WSXM software [31]. The STS spectra were taken by using a lock-in amplifier with a modulation voltage of 20 mV at a frequency of 677 Hz.

Density-functional theory calculations were performed using the generalized gradient approximation for the exchange-correlation potential, the projector augmented-wave method [32,33], and a plane-wave basis set as implemented in the Vienna *Ab initio* Simulation Package (VASP) [34]. Dispersion corrections were made at the van der Waals density-functional level [35,36], with the optB86b functional for the exchange potential (optB86b-vdW) [37,38]. The kinetic energy cutoff for the plane-wave basis was set to 700 eV for the geometric properties of the unit cell of MoS_2 and 550 eV for electronic structure calculations, respectively. Two k meshes of $17 \times 17 \times 5$ and $17 \times 17 \times 1$ were used to sample the first Brillouin zone in the bulk and mono- or few-layered forms, respectively. A vacuum layer of around 17 Å was used in monolayered and few-layered structures. The shape and volume of the unit cell of MoS_2 were fully relaxed until the residual force per atom was less than 0.005 eV/Å. In terms of oxygen-substituting structures, a kinetic energy cutoff of 550 eV and a k mesh of $17 \times 17 \times 1$ were adopted for structure optimization. The shape and volume of the supercell were fixed, but all atoms were fully relaxed until the residual force per atom was less than 0.01 eV/Å. Although the c lattice keeps fixed during the structural optimization, all MoS_2 and MoSO layers are free to move towards the vacuum layer. We summarized the change of interlayer distances (Mo-Mo distances in the c direction) of three fully relaxed O-substituted trilayers in Supplemental Material, Table S1 [39], in which it clearly shows the change of interlayer distances after structural relaxation.

In our experiments, few-layered MoS_2 were grown on HOPG. MoS_2 islands have triangle shapes and exhibit random orientations with respect to the HOPG substrate, but the orientations of each layer in single island are same (Fig. S1) [39]. Atomically smooth terraces with thicknesses from one to nine layers were explicitly identified in the STM image of single-crystal islands, as shown in Fig. 1(d). Figure 1(e) plots the differential conductance (dI/dV) curves associated with the observed terraces as measured by STS, in which one peak was found at -2.15 ± 0.02 V (sample bias corresponding to occupied states) on the first layer of MoS_2, and two peaks were found at -2.5 and -1.8 V on the second layer. The number of peaks increased explicitly with the number of layers, while the energy separation between these peaks decreased accordingly. The evolution of the dI/dV peaks can also be illustrated in the color map in Fig. 1(f), which consists of a series of dI/dV curves acquired along the white line in Fig. 1(d). It shows that the number of peaks (and their energy separation) jumped when crossing terraces, but remained unchanged within the same terrace. The pattern is consistent with Davydov splitting [53,54]. More QWSs will involve in the tunneling process when we perform STS measurements on thicker MoS_2 film. Therefore, for thicker MoS_2 film, more

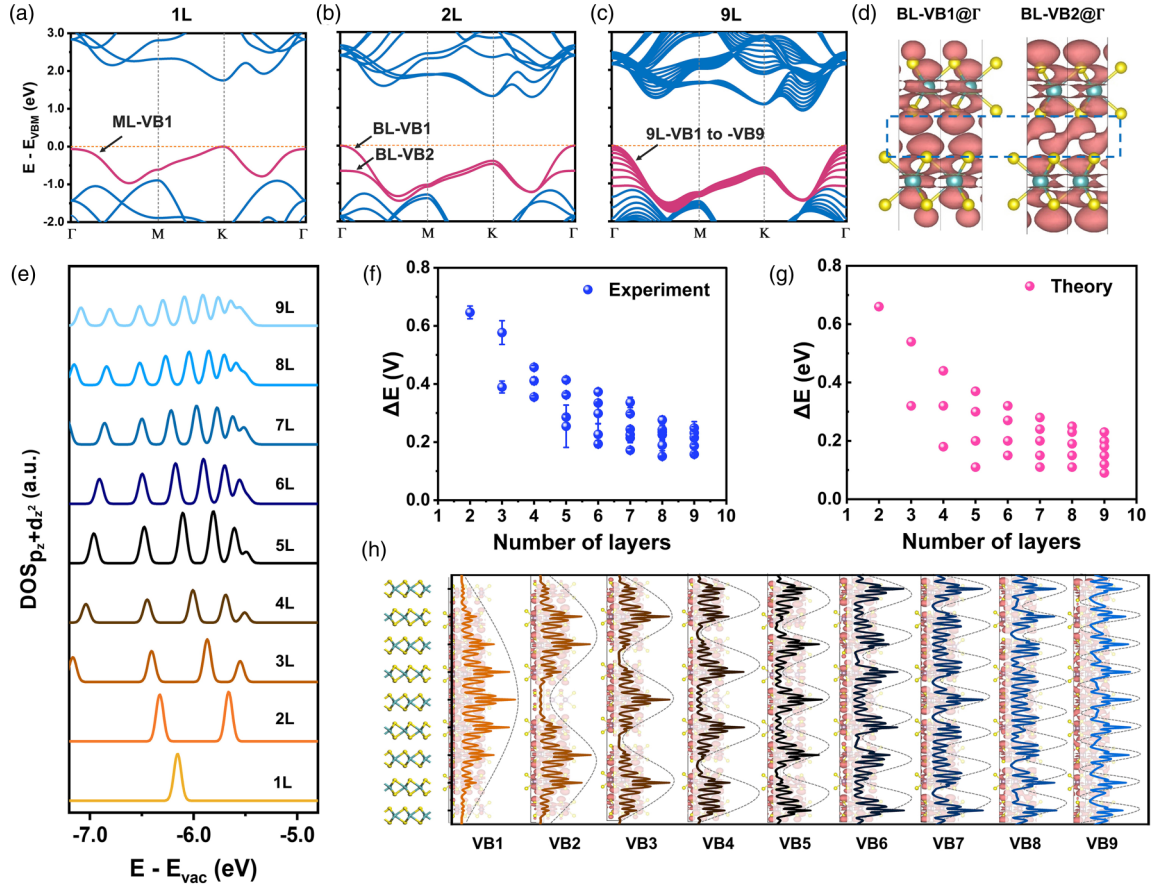

FIG. 2. (a)–(c) DFT calculated band structures of mono-, bi-, and nine-layers MoS_2, respectively. The highest valence band in monolayer MoS_2 (ML-VB1) shows significant splitting when the number of layers increased. (d) Visualized wave-function norms of the two highest valence bands of bilayer MoS_2 (BL-VB1 and BL-VB2) at the Γ point. The isosurface value is 0.001 e/Bohr^3. A blue dashed rectangular box indicates the interlayer region for highlighting the interlayer bonding and antibonding states. (e) The calculated density of states at the Γ point for 1–9-L MoS_2. Since interlayer hybridization mostly comes from the p_z and d_{z^2} orbitals, only these two orbitals were taken into account. To compare with the DOS acquired on the MoS_2 surface in STS, the calculated results presented here are the sum of the first S-Mo-S layer in each structure. (f) and (g) The dependence of the energy interval between adjacent peaks in the dI/dV spectra and density of states at point Γ on the number of layers in 1–9-L MoS_2. The error bars in (f) are obtained according to the full width at half maximum of peaks. (h) Wave-function visualization of the nine highest valence bands at the Γ point of 9-L MoS_2. The solid lines with different colors represent the line profiles of these states perpendicular to the plane, and the corresponding envelope functions show the characteristic wave functions for a finitely deep square potential well.

QWS peaks will occur at lower energy than −3.0 eV (Figs. S2 and S4). The gap of few-layers MoS_2 and the band bending at the step edge shown on STS is consistent with previous studies (Fig. S5) [39]. As illustrated in Fig. 1(b), the valence states of each MoS_2 layer were hybridized to produce discrete valence bands in multilayered structures; thus, we believe that the peaks are quantized 2D QWSs.

Figures 2 and S7 [39] plot the theoretical band structures of layered MoS_2 from 1 to 9 L. The highest valence band of MoS_2 monolayer [ML-VB1 in Fig. 2(a)] have different orbital compositions at the Γ, *M,* and *K* points [Fig. S9(b)]. Particularly, ML-VB1@Γ primarily comprises S p_z and Mo d_{z^2} components, both of which play essential roles in interlayer coupling. BL-VB1 and BL-VB2 in MoS_2 bilayer interact and lift the degeneracy in variable strengths at different *k* points [Fig. 2(b)]. A pair of interlayer bonding and antibonding states were found for BL-VB1/2@Γ [Fig. 2(d)], hybridized through their S p_z orbitals, while no overlap was present at the interlayer region at the *K* and *M* points [Fig. S10(b) [39]]. The hybridization causes an energy separation of 0.66 eV for BL-VB1 and -VB2 at the Γ point, rather pronounced in comparison with those of 0.05–0.08 eV at *M* and *K* points. The two different origins for lifting degeneracy lead to the valence-band maximum moving from the *K* point in the monolayer to the Γ point of the bilayer [16,55–59]. Such hybridization is also supported by a plot of interlayer differential charge density (Fig. S11 [39]), where a covalentlike charge-transfer nature is clearly illustrated. The dispersedly distributed energies of those nine states (9L-VB1 to -VB9) in 9-L MoS_2 within a 1.07-eV range [Fig. 2(c)] indicate that all those bands involve in the hybridization, which is supported by the visualized bonding and antibonding states in Fig. S12 [39]. This unexpectedly strong interlayer hybridization is also reflected by the highly dispersive band which developed along the out-of-plane direction (i.e., Γ-*A* direction) of bulk MoS_2 (Fig. S8 [39]).

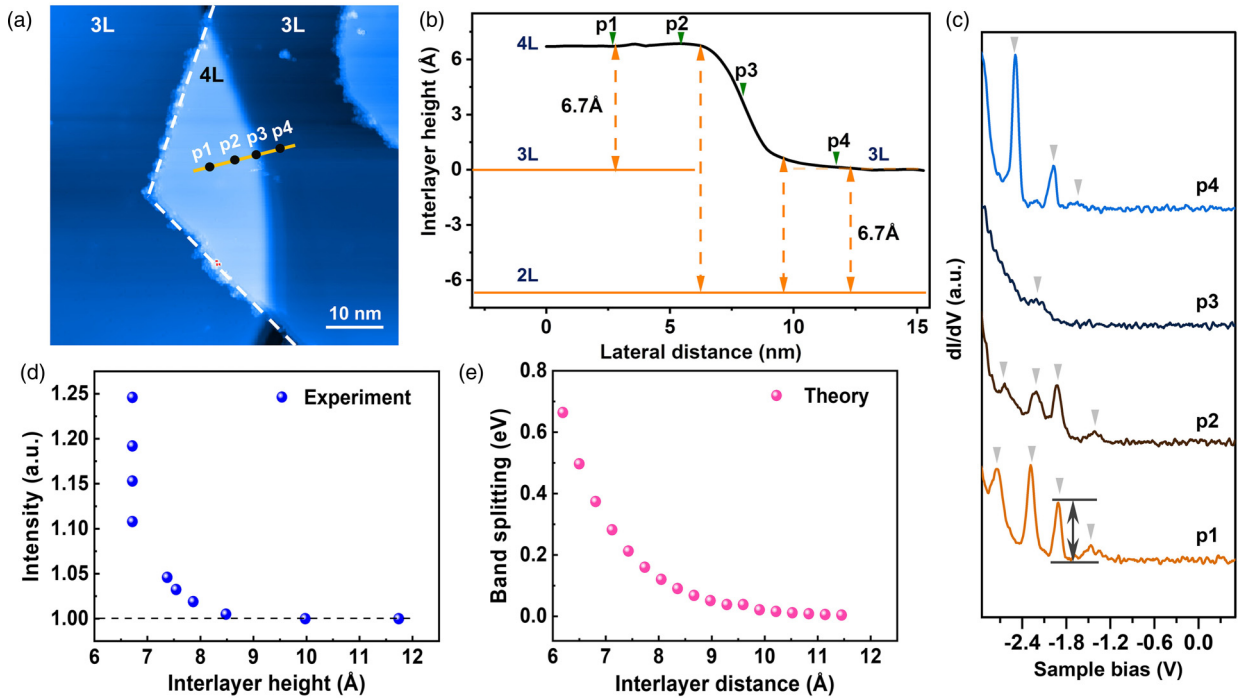

FIG. 3. (a) The STM image of two trilayer MoS_2 in which the left part of one top layer stacks on the other top layer nearby ($60 \times 60\,nm^2$; $V_s = -2.8\,V$, $I_s = 100\,pA$). (b) The black line represents the height line profile along the orange line in (a). Schematic illustration of (a) is shown in the orange line. The double-arrow dashed lines indicate the height between layers. The corresponding positions of the dI/dV spectra (c) are given by the green triangles (p1–p4) in (b). (d) The relationship between interlayer height and peak intensity. The peak intensity is expressed in terms of the peak-to-valley ratio of the second peak, namely the two-way arrow in (c). (e) Dependence of band splitting between subband 1 and subband 2 at the Γ point on the interlayer distance in bilayered MoS_2. The energy interval decreases upon increasing the interlayer distance and becomes zero when the interlayer distance is larger than 10 Å.

Figure 2(e) depicts the projected density of states of these subbands at the Γ point projecting along the p_z and d_{z^2} orbitals of the top S-Mo-S layer, which agrees well with the experimental peaks qualitatively. In Figs. 2(f) and 2(g), the energy positions of the experimental peaks and theoretical subbands are quantitatively plotted as a function of the thickness, and they are in good agreement with each other. Furthermore, we plotted the line profiles of the wave-function norms of VB1 to VB9 in 9-L MoS_2 along the out-of-plane direction [Fig. 2(h)]. The envelope functions show apparent nodes, whose numbers increased from 1 to 9, reflecting the typical characteristic of QWSs. Again, this supports the QWSs induced by interlayer hybridization in MoS_2.

While electronic hybridization governs the formation of QWSs in our case, we infer that the strength of hybridization most likely affects the appearance of the quantum well. This effect was indeed observed in our experiment. Figure 3(a) shows a special region of our MoS_2 sample, in which the top layer of the right trilayer island extends into the neighboring left trilayer island, resulting in a smooth variation in the trilayer and four-layer (2*H* stacking mode) junctions. Near the junction, the apparent height of the top layer continuously varies from 6.7 ∼ 13.0 Å [the line profile in Fig. 3(b)]. This allows us to examine the relationship between the interlayer coupling strength and the appearance of QWSs. Four typical dI/dV curves taken at points 1–4 [Fig. 3(a)] are shown in Fig. 3(c), where points 1 and 2 (4) are at the four (tri)-layer regions, and point 3 is at the transition region with a rather large interlayer height. Although all spectra were obtained on the same atomic layer, the measured LDOSs are quite different. Four pronounced peaks are observed in the spectra of point 1 and 2, which corresponds well to the four-layer thickness. The peak positions are nearly unchanged, but their intensity was slightly reduced at point 2. On the other hand, three peaks were observed in the spectra of point 4. The transition region (point 3) behaves dramatically differently, showing one weak bump at 2.16 ± 0.03 V. This is similar to that of the monolayer in Fig. 1(e) and suggests interlayer decoupling due to the large interlayer height.

We examined the dI/dV spectra around point 3 in more detail by recording more data points from points 2 to 4, where the interlayer height varied from 6.7 to over 10 Å, as shown in Fig. 3(d). The term "peak intensity" expresses the peak-to-valley ratio of the second peak [see the mark on curve p1 in Fig. 3(c)], which becomes weaker with greater interlayer height. If the interlayer height exceeds 8.5 Å, the second peak fades and completely vanishes at roughly 10.0 Å, corresponding to the disappearance of interlayer hybridization. We calculated the band structures of bilayer MoS_2 with various interlayer distances, and the dependence of energy splitting of the highest valence bands (subbands 1 and 2) on the interlayer distance is shown in Fig. 3(e). The splitting of subbands 1 and 2 rapidly decreased as the interlayer distance increased, and reached nearly zero at 10.5 Å, which corresponds to

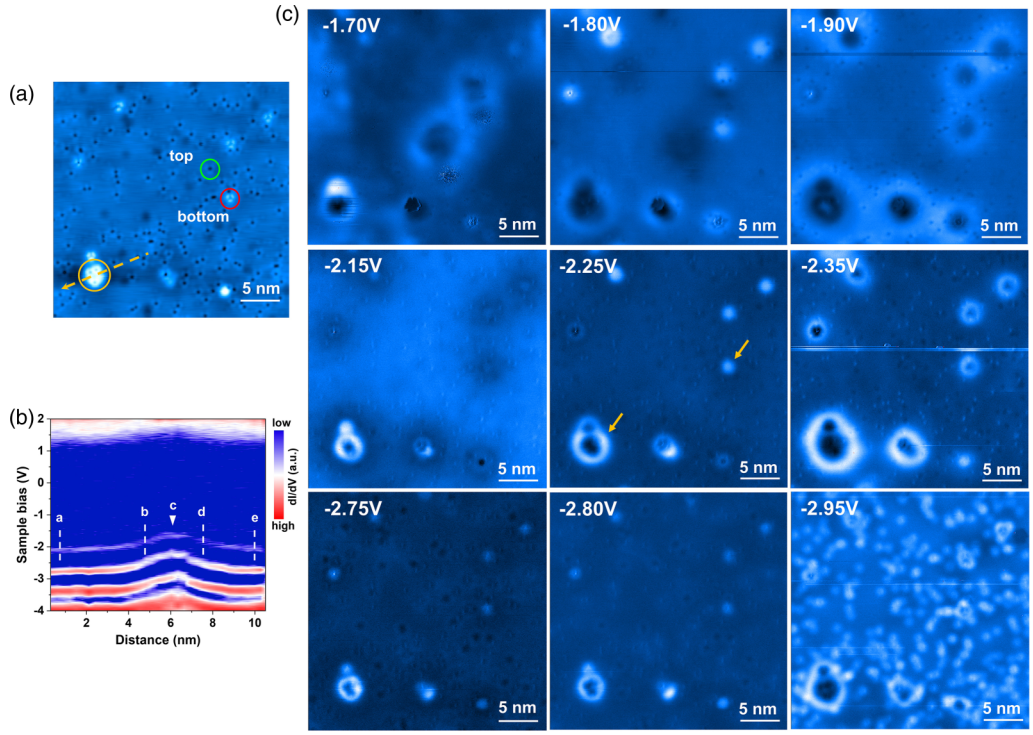

FIG. 4. (a) The STM image of MoS_2 surface ($30 \times 30\,nm^2$; $V_s = -2.8$ V, $I_s = 100$ pA). Two prime defect types (O_s) where oxygen atoms replaced sulfur atoms: dark holes (top O_{top}) and bright petal patterns (bottom O_{bottom}) corresponding to green and red circles can be clearly distinguished. The orange rings encircle three nearest-neighbor O_{bottom} defects. (b) The color map of the dI/dV spectra contains the entire band gap obtained along the dashed line (a few O_{bottom} defects) in (a). (c) Measured dI/dV mappings of (a) at different energies (sample bias; $30 \times 30\,nm^2$). The bright rings with a change in energy appeared near the O_{bottom} defects. The orange arrows indicate the location of bright rings.

the near-complete disappearance of interlayer hybridization in experimental observations. We thus inferred that increasing the interlayer distance largely weakens the interlayer coupling and thus breaks down the 2D quantum well.

While the electronic hybridization among S $3p$ states played a major role in forming QWSs, it is intuitive that substitution of sulfur atoms with other elements could modify the interlayer hybridization and thus tune the emergence of QWSs. In our experiments, we introduced oxygen atoms into few-layered MoS_2 during sample preparation [60]. Figure 4(a) depicts an STM image containing two types of defects on the surface of few-layered MoS_2, namely, predominant dark holes and a few bright petal patterns. The STS measurements (Fig. S13 [39]) showed that the defects decreased the band gap, and there are no in-gap defect states. According to the similar features in STM images and dI/dV spectra of MoS_2 [60,61], as well as WS_2 and $MoSe_2$ [62–64], the defects were determined to be O atoms that replaced S atoms in the top (O_{top}) and bottom (O_{bottom}) sublayers of the surface layer, respectively, and not the S vacancies [29,49,65].

In the dI/dV maps taken at bias voltages from -1.7 to -3.0 V [Fig. 4(c)], we can observe single bright rings surrounding O_{bottom} defects. The rings extend as the energy increases (from -1.70 to -1.90 V) until they disappear, and then begin to extend and disappear again from -2.15 to -2.35 V and from 2.75 to -2.95 V. Such behavior is much more prominent for the three O_{bottom} closely located defects in the bottom left of Figs. 4(a) and 4(c). However, we did not find any rings around the O_{top} defects. To determine the origin of the rings surrounding the O_{bottom} defects, a series of STS measurements were performed along one line across the area with the three defects in Fig. 4(a). The dI/dV curves are plotted as a color map in Fig. 4(b). The three peaks corresponding to QWSs were all gradually upshifted from -1.5 to -3.5 V when the point was near the defect area, which explains the three rounds of appearance-disappearance of the bright rings in the dI/dV maps. The maximum energy shift (0.45 ± 0.04 eV) was obtained at the center of the defect area (Fig. S14 [39]). A similar, but significantly smaller, energy shift of 0.17 $\pm$ 0.02 eV was also observed at the single O_{bottom} defect area (Fig. S13 [39]).

The upward shift of QWSs energies at the O_{bottom} area is usually thought to be a result of band bending due to charge screening at defects on semiconductor surfaces [66]. However, this should be simultaneously observed in both the valence and conductance bands. In our system, however, the conduction band remained nearly unchanged around O_{bottom} [Figs. 4(c) and S14 [39]], which rules it out as possible reason for the energy shift. On the other hand, oxygen and sulfur atoms are isoelectronic, and thus the substitution of S with O should not induce electron doping or screening effects. Considering that the energy upshift of QWSs was not found near O_{top} defects, and a more pronounced energy shift was observed near the three defects, this phenomenon can be qualitatively explained due to the change of the interlayer hybridization by O_{bottom} defects in the top MoS_2 layer.

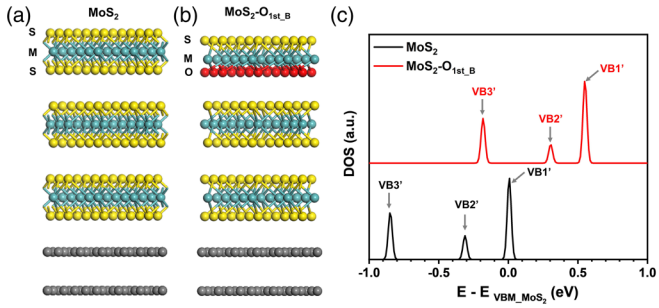

FIG. 5. (a) Atomic structure of bilayer $\sqrt{21} \times \sqrt{21}$ graphene (gray balls) supported trilayer $\sqrt{13} \times \sqrt{13}$ MoS_2. (b) A sublayer of S atoms is substituted by O atoms. The red balls represent O atoms. (c) Total DOS at the Γ point of 3-L unit cell of MoS_2 and O_{1st_B} (the subscript indicates which sublayer is substituted). The energy levels have been aligned by the Fermi levels of graphene-supported heterobilayers.

To confirm this, we carried out DFT calculations to examine the role of O substitution. Figure 5(a) shows an atomic model of graphite-supported trilayered MoS_2, while Fig. 5(b) depicts an extreme case where the bottom S sublayer was fully replaced with O atoms. Changes of interlayer distances (Mo-Mo distances in the *c* direction) after substitution are shown in Table S1. In the pristine trilayer, the valence band splits into three subbands at the Γ point, denoted as VB1′ to VB3′ (Fig. S7 [39]), whose LDOS at the Γ point are plotted in Fig. 5(c). In terms of the full substitution model (O_{1st_B}), the energies of VB1′ to VB3′ collectively shift upward by 0.54–0.67 eV [Fig. 5(c)]. We must emphasize that the model used in our calculations is an extreme case. In our experiments, the energy upshifts of QWSs occur in regions with only a few defects, but their values are comparable with the calculations. Combining experiments with calculations results, we can conclude that when the bottom S atoms of the first layer in trilayer MoS_2 are substituted by O atoms, the interactions between the first layer and second layer are substantially changed. This influences the electron propagation in the quantum well and modifies the intrinsic QWSs. Moreover, considering the different energy shifts observed near single-defect and three-defects areas, we think the degree of energy shift of QWSs can be well tuned by the density and distribution of O_{bottom} defects.

In summary, combining STM/STS measurements and DFT calculations, we detected quantized states on few-layered MoS_2 in real space strictly corresponding to the number of layers. This confirms the existence of 2D QWSs and strong interlayer hybridization in MoS_2. Moreover, we demonstrate two strategies to modify the QWSs in MoS_2. First, we show that QWSs can be tuned by the interlayer distance. Second, we found that the substitution of O for bottom S atoms in the top MoS_2 layer induces a remarkable energy shift in the QWSs. The direct observation and manipulation of QWSs in vdW layered MoS_2 are likely to be generalized to other layered vdW materials. As such, our findings will be helpful to understand many physical phenomena in vdW materials, such as optical transitions [67], catalysis [68], and magnetism [69], and promote their applications in electronics and optoelectronics.

This work was supported from Beijing Municipal Natural Science Foundation (Grant No. Z180007), the Ministry of Science and Technology (MOST) of China (Grant No. 2018YFE0202700), the National Natural Science Foundation of China (Grants No. 12134019, No. 11825405, No. 61674171, No. 11974422, No. 61888102, and No. 11834017), the Strategic Priority Research Program of Chinese Academy of Sciences (Grants No. XDB30000000 and No. XDB0000000), the Fundamental Research Funds for the Central Universities, China, and the Research Funds of Renmin University of China (Grants No. 16XNLQ01 and No. 19XNQ025), and the Research Program of Beijing Academy of Quantum Information Sciences (Grant No. Y18G11). L.W. was supported by the Outstanding Innovative Talents Cultivation Funded Programs 2021 of Renmin University of China.

[1] Y. Qi, X. C. Ma, P. Jiang, S. H. Ji, Y. S. Fu, J.-F. Jia, Q.-K. Xue, and S. B. Zhang, Appl. Phys. Lett. **90**, 013109 (2007).
[2] J. J. Paggel, C. M. Wei, M. Y. Chou, D.-A. Luh, T. Miller, and T.-C. Chiang, Phys. Rev. B **66**, 233403 (2002).
[3] J. Kim, S. Y. Qin, Y. Zhang, W. G. Zhu, and C.-K. Shih, Surf. Sci. **632**, 174 (2015).
[4] Y. Jiang, K. H. Wu, J. Ma, B. Wu, E. G. Wang, and Ph. Ebert, Phys. Rev. B **76**, 235434 (2007).
[5] M. M. Özer, Y. Jia, Z. Y. Zhang, J. R. Thompson, and H. H. Weitering, Science **316**, 1594 (2007).
[6] Y. Guo, Y. F. Zhang, X. Y. Bao, T. Z. Han, Z. Tang, L. X. Zhang, W. G. Zhu, E. G.Wang, Q. Niu, Z. Q. Qiu, J. F. Jia, Z. X. Zhao, and Q. K. Xue, Science **306**, 1915 (2004).
[7] L. Aballe, A. Barinov, A. Locatelli, S. Heun, and M. Kiskinova, Phys. Rev. Lett. **93**, 196103 (2004).
[8] M. Milun, P. Pervan, and D. P. Woodruff, Rep. Prog. Phys. **65**, 99 (2002).
[9] X. C. Ma, P. Jiang, Y. Qi, J. F. Jia, Y. Yang, W. H. Duan, W.-X. Li, X. H. Bao, S. B. Zhang, and Q.-K. Xue, Proc. Natl. Acad. Sci. USA **104**, 9204 (2007).
[10] Q. H. Wang, K. K.-Zadeh, A. Kis, J. N. Coleman, and M. S. Strano, Nat. Nanotechnol. **7**, 699 (2012).
[11] Y. W. Zhang, H. Li, H. M. Wang, R. Liu, S.-L. Zhang, and Z.-J. Qiu, ACS Nano **9**, 8514 (2015).
[12] C. Murray, C. van Efferen, W. Jolie, J. A. Fischer, J. Hall, A. Rosch, A. V. Krasheninnikov, H.-P. Komsa, and T. Michely, ACS Nano **14**, 9176 (2020).
[13] H. Y. Zhang, C. H. Bao, Z. Y. Jiang, K. N. Zhang, H. Li, C. Y. Chen, J. Avila, Y. Wu, W. H. Duan, M. C. Asensio, and S. Y. Zhou,, Nano Lett **18**, 4664 (2018).
[14] W. C. Jin, P.-C. Yeh, N. Zaki, D. T. Zhang, J. T. Sadowski, A. A.-Mahboob, A. M. van der Zande, D. A. Chenet, J. I. Dadap, I. P. Herman, P. Sutter, J. Hone, and R. M. Osgood, Jr., Phys. Rev. Lett. **111**, 106801 (2013).
[15] P. Schmidt, F. Vialla, S. Latini, M. Massicotte, K.-J. Tielrooij, S. Mastel, G. Navickaite, M. Danovich, D. A. R.-Tijerina, C. Yelgel, V. Fal'ko, K. S. Thygesen, R. Hillenbrand, and F. H. L. Koppens, Nat. Nanotechnol. **13**, 1035 (2018).
[16] K. F. Mak, C. Lee, J. Hone, J. Shan, and T. F. Heinz, Phys. Rev. Lett. **105**, 136805 (2010).

[17] Y. Zhang, M. M. Ugeda, C. H. Jin, S.-F. Shi, A. J. Bradley, A. Martín-Recio, H. Ryu, J. Kim, S. J. Tang, Y. Kim, B. Zhou, C. Hwang, Y. L. Chen, F. Wang, M. F. Crommie, Z. Hussain, Z.-X. Shen, and S.-K. Mo, Nano Lett. **16**, 2485 (2016).

[18] H. C. Diaz, J. Avila, C. Y. Chen, R. Addou, M. C. Asensio, and M. Batzill, Nano Lett. **15**, 1135 (2015).

[19] N. R. Wilson, P. V. Nguyen, K. Seyler, P. Rivera, A. J. Marsden, Z. P. L. Laker, G. C. Constantinescu, V. Kandyba, A. Barinov, N. D. M. Hine, X. D. Xu, and D. H. Cobden, Sci. Adv. **3**, e1601832 (2017).

[20] L. K. Li, J. Kim, C. H. Jin, G. J. Ye, D. Y. Qiu, F. H. da Jornada, Z. W. Shi, L. Chen, Z. C. Zhang, F. Y. Yang, K. Watanabe, T. Taniguchi, W. C. Ren, S. G. Louie, X. H. Chen, Y. B. Zhang, and F. Wang, Nat. Nanotechnol. **12**, 21 (2017).

[21] V. Tayari, N. Hemsworth, I. Fakih, A. Favron, E. Gaufrès, G. Gervais, R. Martel, and T. Szkopek, Nat. Commun. **6**, 7702 (2015).

[22] T. Vincent, E. Voloshina, S. Pons, S. Simon, M. Fonin, K. Wang, B. Paulus, D. Roditchev, Yuriy Dedkov, and S. Vlaic, J. Phys. Chem. Lett. **11**, 1594 (2020).

[23] Z. X. Hu, X. H. Kong, J. S. Qiao, B. Normand, and W. Ji, Nanoscale **8**, 2740 (2016).

[24] Y. D. Zhao, J. S. Qiao, P. Yu, Z. X. Hu, Z. Y. Lin, S. P. Lau, Z. Liu, W. Ji, and Y. Chai, Adv. Mater. **28**, 2399 (2016).

[25] Y. D. Zhao, J. S. Qiao, Z. H. Yu, P. Yu, K. Xu, S. P. Lau, W. Zhou, Z. Liu, X. R. Wang, W. Ji, and Y. Chai, Adv. Mater. **29**, 1604230 (2017).

[26] R. Ganatra and Q. Zhan, ACS Nano **8**, 4074 (2014).

[27] J. A. Miwa, S. Ulstrup, S. G. Sørensen, M. Dendzik, A. G. Čabo, M. Bianchi, J. V. Lauritsen, and P. Hofmann, Phys. Rev. Lett. **114**, 046802 (2015).

[28] A. Bruix, J. A. Miwa, N. Hauptmann, D. Wegner, S. Ulstrup, S. S. Grønborg, C. E. Sanders, M. Dendzik, A. G. Čabo, M. Bianchi, J. V. Lauritsen, A. A. Khajetoorians, B. Hammer, and P. Hofmann, Phys. Rev. B **93**, 165422 (2016).

[29] C.-P. Lu, G. Li, J. Mao, L.-M. Wang, and E. Y. Andrei, Nano Lett. **14**, 4628 (2014).

[30] X. Zhou, K. Kang, S. Xie, A. Dadgar, N. R. Monahan, X.-Y. Zhu, J. Park, and A. N. Pasupathy, Nano Lett. **16**, 3148 (2016).

[31] I. Horcas, R. Fernández, J. M. G.-Rodríguez, J. Colchero, J. Gómez.-Herrero, and A. M. Baro, Rev. Sci. Instrum. **78**, 013705 (2007).

[32] P. E. Blöchl, Phys. Rev. B **50**, 17953 (1994).

[33] G. Kresse and D. Joubert, Phys. Rev. B **59**, 1758 (1999).

[34] G. Kresse and J. Furthmüller, Phys. Rev. B **54**, 11169 (1996).

[35] M. Dion, H. Rydberg, E. Schröder, D. C. Langreth, and B. I. Lundqvist, Phys. Rev. Lett. **92**, 246401 (2004).

[36] K. Lee, É. D. Murray, L. Kong, B. I. Lundqvist, and D. C. Langreth, Phys. Rev. B **82**, 081101 (2010).

[37] J. Klimeš, D. R. Bowler, and A. Michaelides, Phys. Rev. B **83**, 195131 (2011).

[38] J. Klimeš, D. R. Bowler, and A. Michaelides, J. Phys.: Condens. Matter **22**, 022201 (2009).

[39] See Supplemental Material at http://link.aps.org/supplemental/10.1103/PhysRevB.105.L081404, which includes Refs. [12,40–52], for details of auxiliary data.

[40] N. Ehlen, J. Hall, B. V. Senkovskiy, M. Hell, J. Li, A. Herman, D. Smirnov, A. Fedorov, V. Y. Voroshnin, G. D. Santo, L. Petaccia, T. Michely, and A. Grüneis, 2D Mater. **6**, 011006 (2019).

[41] N. Krane, C. Lotze, J. M. Lager, G. Reecht, and K. J. Franke, Nano Lett. **16**, 5163 (2016).

[42] D. J. Trainer, A. V. Putilov, B. Wang, C. Lane, T. Saari, T.-R. Chang, H.-T. Jeng, H. Lin, X. Xi, J. Nieminen, A. Bansil, and M. Iavarone, J. Phys. Chem. Solids **128**, 325 (2019).

[43] Y. L. Huang, Y. F. Chen, W. J. Zhang, S. Y. Quek, C. -H. Chen, L. -J. Li, W. -T. Hsu, W. -H. Chang, Y. J. Zheng, W. Chen, and A. T. S. Wee, Nat. Commun. **6**, 6298 (2015).

[44] C. H. Yan, X. Dong, C. H. Li, and L. Li, Nanotechnology **29**, 195704 (2018).

[45] X. Liu, I. Balla, H. Bergeron, G. P. Campbell, M. J. Bedzyk, and M. C. Hersam, ACS Nano **10**, 1067 (2015).

[46] M.-H. Chiu, C. D. Zhang, H.-W. Shiu, C.-P. Chuu, C.-H. Chen, C.-Y. S. Chang, C.-H. Chen, M.-Y. Chou, C.-K. Shih, and L.-J. Li, Nat. Commun. **6**, 7666 (2015).

[47] C. Zhang, A. Johnson, C.-L. Hsu, L.-J. Li, and C.-K. Shih, Nano Lett. **14**, 2443 (2014).

[48] Z.-H. Huang, M. Weimer, and R. E. Allen, Phys. Rev. B **48**, 15068 (1993).

[49] M. H. Naik and M. Jain, Phys. Rev. Mater. **2**, 084002 (2018).

[50] H. Lin, J. Lagoute, V. Repain, C. Chacon, Y. Girard, J.-S. Lauret, F. Ducastelle, A. Loiseau, and S. Rousset, Nat. Mater. **9**, 235 (2010).

[51] M. McEllistrem, G. Haase, D. Chen, and R. J. Hamers, Phys. Rev. Lett. **70**, 2471 (1993).

[52] R. M. Feenstra, Y. Dong, M. P. Semtsiv, and W. T. Masselink, Nanotechnology **18**, 044015 (2007).

[53] A. S. Davydov, Sov. Phys. Usp. **7**, 145 (1964).

[54] G. Froehlicher, E. Lorchat, F. Fernique, C. Joshi, A. Molina-Sánchez, L. Wirtz, and S. Berciaud, Nano Lett. **15**, 6481 (2015).

[55] A. Kuc, N. Zibouche, and T. Heine, Phys. Rev. B **83**, 245213 (2011).

[56] A. Splendiani, L. Sun, Y. Zhang, T. Li, J. Kim, C.-Y. Chim, G. Galli, and F. Wang, Nano Lett. **10**, 1271 (2010).

[57] H. S. S. R. Matte, A. Gomathi, A. K. Manna, D. Late, R. Datta, S. Pati, and C. Rao, Angew. Chem. Int. Ed. **49**, 4059 (2010).

[58] T. Li and G. Galli, J. Phys. Chem. C **111**, 16192 (2007).

[59] S. Lebègue and O. Eriksson, Phys. Rev. B **79**, 115409 (2009).

[60] J. Tang, Z. Wei, Q. Q. Wang, Y. Wang, B. Han, X. M. Li, B. Y. Huang, M. Z. Liao, J. Y. Liu, N. Li, Y. C. Zhao, C. Shen, Y. T. Guo, X. D. Bai, P. Gao, W. Yang, L. Chen, K. H. Wu, R. Yang, D. X. Shi, and G. Y. Zhang, Small **16**, 2004276 (2020).

[61] J. Pető, T. Ollár, P. Vancsó, Z. I. Popov, G. Z. Magda, G. Dobrik, C. Y. Hwang, P. B. Sorokin, and L. Tapasztó, Nat. Chem. **10**, 1246 (2018).

[62] B. Schuler, J.-H. Lee, C. Kastl, K. A. Cochrane, C. T. Chen, S. R.-Abramson, S. J. Yuan, E. van Veen, R. Roldan, N. J. Borys, R. J. Koch, S. Aloni, A. M. Schwartzberg, D. F. Ogletree, J. B. Neaton, and A. Weber-Bargioni, ACS Nano **13**, 10520 (2019).

[63] S. Barja, S. R. Abramson, B. Schuler, D. Y. Qiu, A. Pulkin, S. Wickenburg, H. Ryu, M. M. Ugeda, C. Kastl, C. Chen, C. Y. Hwang, A. Schwartzberg, S. Aloni, S. K. Mo, D. F. Ogletree, M. F. Crommie, O. V. Yazyev, S. G. Louie, J. B. Neaton, and A. Weber-Bargioni, Nat. Commun. **10**, 3382 (2019).

[64] B. Schuler, D. Y. Qiu, S. Refaely-Abramson, C. Kastl, C. T. Chen, S. Barja, R. J. Koch, D. F. Ogletree, S. Aloni, A. M. Schwartzberg, J. B. Neaton, S. G. Louie, and A. Weber-Bargioni, Phys. Rev. Lett. **123**, 076801 (2019).

[65] R. Addou, S. McDonnell, D. Barrera, Z. Guo, A. Azcatl, J. Wang, H. Zhu, C. L. Hinkle, M. Quevedo-Lopez, H. N.

Alshareef, L. Colombo, J. W. P. Hsu, and R. M. Wallace, ACS Nano **9**, 9124 (2015).

[66] T. Le. Quang, K. Nogajewski, M. Potemski, M. T. Dau, M. Jamet, P. Mallet, and J.-Y. Veuillen, 2D Mater. **5**, 035034 (2018).

[67] M. Elborg, T. Noda, T. Mano, and Y. Sakuma, AIP Adv. **6**, 065208 (2016).

[68] T. Q. Niu, J. Lu, X. G. Jia, Z. Xu, M.-C. Tang, D. Barrit, N. Y. Yuan, J. N. Ding, X. Zhang, Y. Y. Fan, T. Luo, Y. L. Zhang, D.-M. Smilgies, Z. K. Liu, A. Amassian, S. Y. Jin, K. Zhao, and S. Z. Liu, Nano Lett. **19**, 7181 (2019).

[69] S. C. Hong, J. I. Lee, and R. Wu, Phys. Rev. B **75**, 172402 (2007).